MATERIALS SCIENCE

Morphology controls the thermoelectric power factor of a doped semiconducting polymer

Shrayesh N. Patel,[1]* Anne M. Glaudell,[1,2] Kelly A. Peterson,[2] Elayne M. Thomas,[2] Kathryn A. O'Hara,[2] Eunhee Lim,[2] Michael L. Chabinyc†

The electrical performance of doped semiconducting polymers is strongly governed by processing methods and underlying thin-film microstructure. We report on the influence of different doping methods (solution versus vapor) on the thermoelectric power factor (PF) of PBTTT molecularly p-doped with F_nTCNQ (n = 2 or 4). The vapor-doped films have more than two orders of magnitude higher electronic conductivity (σ) relative to solution-doped films. On the basis of resonant soft x-ray scattering, vapor-doped samples are shown to have a large orientational correlation length (OCL) (that is, length scale of aligned backbones) that correlates to a high apparent charge carrier mobility (μ). The Seebeck coefficient (α) is largely independent of OCL. This reveals that, unlike σ, leveraging strategies to improve μ have a smaller impact on α. Our best-performing sample with the largest OCL, vapor-doped PBTTT:F_4TCNQ thin film, has a σ of 670 S/cm and an α of 42 μV/K, which translates to a large PF of 120 μW m^{-1} K^{-2}. In addition, despite the unfavorable offset for charge transfer, doping by F_2TCNQ also leads to a large PF of 70 μW m^{-1} K^{-2}, which reveals the potential utility of weak molecular dopants. Overall, our work introduces important general processing guidelines for the continued development of doped semiconducting polymers for thermoelectrics.

INTRODUCTION

Controlling the electrical doping of organic semiconductors is critical to the performance of organic electronic devices (*1*). Doped semiconducting polymers can serve as conductive interlayers for organic light-emitting diodes (OLEDs) (*2*) and solar cells (*2*, *3*) and can improve the performance of organic thin-film transistors (OTFTs) (*4*). One emerging application of doped semiconducting polymers involves organic thermoelectrics—materials that interconvert heat and electricity (*5*–*7*). The solution processability of semiconducting polymers provides the opportunity to use roll-to-roll processing and printing technologies for new classes of thermoelectric modules where the legs are thin films in rolled or corrugated designs (*8*–*13*). To realize the potential of semiconducting polymers for thermoelectrics, however, the relationship between processing and the resulting thermoelectric properties must be better understood.

All of the physical properties of a material that define its thermoelectric performance depend on carrier density (n), including electrical conductivity (σ), Seebeck coefficient (or thermopower) (α), and thermal conductivity (κ) (*14*). The thermal-to-electrical energy conversion efficiency is related to the dimensionless figure of merit, $ZT = \alpha^2\sigma T/\kappa$, where T is the temperature in Kelvin and $\alpha^2\sigma$ is the power factor (PF). Optimizing ZT is quite challenging because as n increases, σ and κ increase while α decreases (*14*). Organic semiconductors frequently have imperfect ordering in thin films, leading to an electronic structure that depends strongly on their morphology (*15*). Because processing methods widely vary in many studies of thermoelectric performance, it is difficult to form clear connections between morphology and thermoelectric performance (*7*).

Here, we elucidate the connection between thin-film microstructure and thermoelectric transport properties (σ and α) of p-doped poly(2,5-bis(3-tetradecylthiophen-2-yl)thieno[3,2-*b*]thiophene) (PBTTT). We focus on p-doping with organic acceptors [2,3,5,6-tetrafluoro-7,7,8,8-tetracyanoquinodimethane (F_4TCNQ) and 2,5-difluoro-7,7,8,8-tetracyanoquinodimethane (F_2TCNQ)] introduced either in solution or from the vapor phase (Fig. 1). The results of our experiments demonstrate how different processing and doping methods affect the thermoelectric PF. In particular, we find that alignment of ordered domains is the critical factor leading to higher σ without lowering α, thereby leading to enhancements in the PF. Using these methods, we have found a PF of 120 μW m^{-1} K^{-2} for PBTTT:F_4TCNQ, which is among the highest reported values for semiconducting polymers (*7*).

The σ value of semiconducting polymers is related to the product of the carrier concentration (n) and carrier mobility (μ). However, because of electronic disorder, the apparent μ of a material will depend on n because of the occupancy of electronic states with varying mobility (*16*–*19*). Through advances in molecular design and processing, solution-processable semiconducting polymers, such as PBTTT, have high charge carrier mobilities (μ > 1 cm^2/V s) in field-effect transistors (*20*). These studies have revealed that the degree of electronic and structural disorder strongly influences μ (*21*, *22*). In field-effect measurements, conduction occurs very close (within ~1 nm) to the polymer-dielectric interface. The microstructure is generally described as (para)crystalline π-stacked domains interconnected by tie chains (*21*). Electrically doped films may require high concentrations of dopant in the bulk (for example, >1 dopant per 10 monomers), which lead to strong perturbations of the morphology and structure relative to pristine films. Whether processing methods that lead to high field-effect μ also lead to high-bulk σ has not been well studied.

The ability to tune the electronic structure of small-molecule organic acceptors (*23*) has resulted in versatile p-type dopants for semiconducting polymers (*16*, *24*–*26*). Electron acceptors have been traditionally co-deposited with molecular organic donors to generate organic charge transfer salts and metals (*27*–*29*). Mixing an organic acceptor into a polymer leads to an integer charge transfer if the

[1]Materials Research Laboratory, University of California, Santa Barbara, Santa Barbara, CA 93106, USA. [2]Materials Department, University of California, Santa Barbara, Santa Barbara, CA 93106, USA.
*Present address: Institute for Molecular Engineering, University of Chicago, 5640 South Ellis Avenue, Chicago, IL 60637, USA.
†Corresponding author. Email: mchabinyc@engineering.ucsb.edu

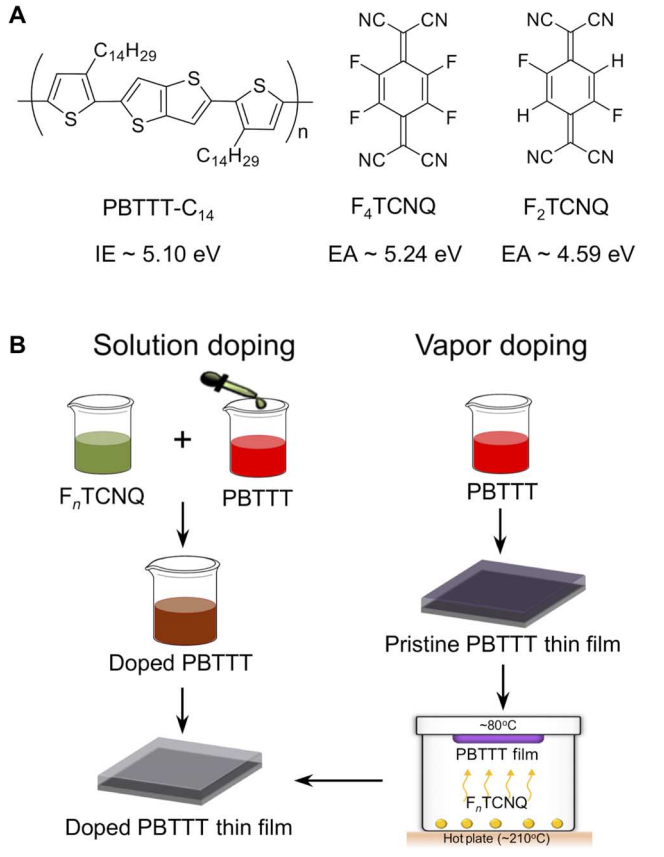

Fig. 1. Chemical structure and doping process. (**A**) Chemical structure of PBTTT and F_nTCNQ (n = 2 or 4) and the corresponding IE or EA. (**B**) Solution and vapor doping routes used to achieve doped films.

offset between HOMO (highest occupied molecular orbital) [ionization energy (IE)] of the polymer and LUMO (lowest unoccupied molecular orbital) [electron affinity (EA)] of the acceptor is sufficient to provide a thermodynamic driving force for electron transfer (Fig. 1) (*16*, *30*–*32*).

How a dopant is incorporated into a semiconducting polymer is critical in dictating the resulting charge transport properties (*33*–*37*). Achieving high σ (>10 S/cm) requires relatively high charge carrier concentrations (>10^{19}/cm^3) due to the observed superlinear increase in conductivity in many materials (*16*, *30*). If a dopant is added to the casting solution, this concentration requires as much as 10 weight % (wt %) relative to the monomer in the solution, which can be difficult because of solubility limits of neutral organic acceptors (*26*). Although chain aggregation appears to aid in efficient charge transfer in some cases (*32*), highly charged polymers can gel or precipitate from solution (*38*). Consequently, one must take great care in determining optimal casting concentrations and temperatures that lead to macroscopically homogenous films (*35*, *38*). Alternatively, first casting a neat film from solution and then subsequently doping has emerged as a versatile route to yield macroscopic homogenous films with high σ (*33*, *35*–*37*). For example, depositing a thin layer of organic acceptor from the vapor phase can lead to diffusion of the dopant into the organic semiconductor (*37*, *39*) and solid-state charge transfer to generate highly conductive films (*37*). Recently, it has been shown that doping spin-coated neat thiophene-based polymers either from the vapor phase (*33*, *37*) or through sequential solution casting (*35*, *36*) can lead to higher σ relative to films cast from a polymer/dopant solution. For example, vapor doping a predeposited PBTTT with F_4TCNQ results in a σ of ~250 S/cm, which is nearly two orders of magnitude higher relative to a solution-doped film with a similar concentration of F_4TCNQ (*37*). The general explanation for the enhancement in σ is related to an overall better macroscopic film quality establishing the underlying microstructure for more efficient charge transport (*35*–*37*). Although these explanations describe enhancement in σ, it is unclear how more efficient charge transport influences the overall thermoelectric properties of semiconducting polymers.

Here, we examine how morphology affects the bulk σ and α of PBTTT. PBTTT is a solution-processable polymer, where the field-effect mobility, crystal structure, and morphology have been well characterized for neat films (*40*–*45*), providing a strong foundation to study how molecular doping influences the morphology and charge transport. In addition, PBTTT has an accessible liquid crystalline transition temperature above ~140°C, which permits thermal processing to enhance local and long-range order (*40*–*42*). Using PBTTT and other thiophene-based polymers, we have previously discovered an empirical connection between electrical conductivity and thermopower across a range of doping methods (*33*, *34*). This broad correlation has been modeled as a result of the electronic density of states (DOS) and energy-dependent mobility, but the connection with morphology has not been made clear. Here, we use PBTTT as a model system to demonstrate how the correlation of alignment in ordered domains at the nanoscale dominates the resulting σ at high n. These results suggest a pathway to increase the thermoelectric PF of semiconducting polymers.

RESULTS AND DISCUSSION

Processing doped films of PBTTT

We prepared highly conductive thin films of PBTTT using different processing methods, with the dopant added in solution or infiltrated from the vapor phase (Fig. 1). A detailed procedure can be found in Materials and Methods, and we outline the critical differences here. We specifically focused on the limit of high doping to determine the connection between morphology and thermoelectric transport properties. For solution doping, 10 wt % of F_4TCNQ relative to PBTTT [molar ratio (MR) of ~1 dopant to 4 monomers] was added to a solution of PBTTT. We have previously found that this composition is near the maximum possible to readily form continuous thin films during spin casting (*38*). The solution was spin-coated to obtain a doped thin film in a N_2 environment and annealed at 150°C for 10 min to remove the solvent. These conditions were used to minimize weight loss of F_4TCNQ from the film (*38*) while also being above the liquid crystalline (LC) transition temperature of the neat polymer. The same processing conditions were used with solution-doped samples, where the dopant was F_2TCNQ. The typical thicknesses of solution-doped films were 40 to 50 nm. To form films doped by infiltration of F_4TCNQ and F_2TCNQ from the vapor phase, we exposed spin-coated films of PBTTT (21 ± 4 nm) prepared using different thermal treatments to the vapor of each compound. In a N_2-filled glove box, we deposited the dopants by placing the samples underneath the lid of a sealed jar containing a few milligrams of dopant. The bottom of the jar was heated to ~210°C, which led to a rise in temperature of the substrate, which was located underneath the lid for the jar, to 75° to 85°C. These temperatures are below the LC transition of PBTTT and are known not to cause substantial changes in the structural order

and charge mobility in OTFTs (*41*). The samples were exposed to the vapor for 10 min, which was sufficient to reach concentrations of F_4TCNQ in PBTTT films comparable to the solution-doped films.

Changes in processing increase electrical conductivity

Efficient charge transfer occurs between PBTTT and F_4TCNQ using both vapor- and solution-based doping. Ultraviolet-visible near-infrared (UV-vis-NIR) spectroscopy shows that neat poly(2,5-bis(3-tetradecylthiophen-2-yl)thieno[3,2-*b*]thiophene) (PBTTT-C_{14}) thin film has a main absorption peak at ~2.2 eV and a shoulder at ~2.1 eV that is bleached upon doping. New absorption peaks appear at 1.41 and 1.60 eV upon introduction of F_4TCNQ and are assigned to its anion radical (*16*, *25*, *37*). The spectral features for the F_4TCNQ radical anion absorption are similar to those in poly(3-hexylthiophene) (P3HT):F_4TCNQ films and have comparable absorptivity for heavily doped films (*35*). A subband gap transition for positive polarons of PBTTT is observed at ~0.5 eV (fig. S2), but the precise position of polaronic features between 1 and 2 eV is difficult to assign because of the strong absorption peaks of the F_4TCNQ anion radical. We observe no significant differences between UV-vis-NIR spectra between vapor-doped as-cast and annealed films, indicating that the annealing step does not change the concentration of F_4TCNQ in the film (fig. S3). A comparison of the main absorption of PBTTT (~2.2 eV) for the vapor-doped film relative to the solution-doped film reveals more bleaching in the former (a factor of 0.78 lower peak area) and also a slightly higher absorbance of F_4TCNQ radical anion. This lower peak area translates to a slightly higher MR of 0.3 relative to the MR of 0.25 in the solution-doped film (*37*).

Strikingly large differences in σ are found between vapor- and solution-doped samples despite this small difference in MR of the dopant. Electrical conductivity measurements (Table 1) indicate 65 times higher σ for the vapor-doped PBTTT:F_4TCNQ annealed film (σ = 220 ± 0.02 S/cm) relative to the solution-doped PBTTT:F_4TCNQ annealed film (σ of 3.51 ± 0.05 S/cm). We observe a similar trend in as-cast films, where σ = 114.1 ± 0.5 S/cm for the vapor-doped film and σ = 2.08 ± 0.01 S/cm for the solution-doped film. Knowing that both doping methods yield comparable carrier concentrations, the large difference in σ must be related to the apparent μ, which is calculated to be ~2.5 and ~0.040 cm^2/V s for the vapor-doped annealed film and the solution-doped annealed film, respectively (assuming F_4TCNQ is fully ionized and all charges are free carriers). The higher apparent μ with vapor-doped films is consistent with Hall effect mobility measurements on vapor-doped PBTTT:F_4TCNQ, which was revealed to be ~2 cm^2/V s (*37*). Two possible factors that can contribute to the difference in apparent μ are differences in local energetic disorder or the long-range morphology.

To determine whether the enhancement in σ was unique to F_4TCNQ, we also examined samples doped with F_2TCNQ. The intermediate fluorination level of F_2TCNQ results in an EA of ~4.59 eV (*46*), which is expected to result in an unfavorable offset for charge transfer with PBTTT (IE, ~5.10 eV) in isolated materials compared to F_4TCNQ (EA, ~5.24 eV). Note that charge transfer is dictated not only by the offset between EA and IE but also by the electrostatic interaction in solids (*47*). Although the EA of F_2TCNQ is lower than the IE of PBTTT-C_{14}, integer charge transfer is indicated by the presence of F_2TCNQ radical anion peaks at 1.43 and 1.62 eV (Fig. 2). Similar observations have been made for structurally similar weak dopants with P3HT (*26*). For both doping methods, PBTTT:F_2TCNQ as-cast films yield a large decrease in the primary absorption, but only the vapor-doped film has a small red shift. In contrast to F_4TCNQ, because of the relatively high vapor pressure of F_2TCNQ, we observe significant dedoping of solution-doped PBTTT:F_2TCNQ films when thermally annealing at 150°C in N_2 environment (fig. S2). The MR in the casting solution is ~0.28 F_2TCNQ per monomer of PBTTT, similar to the solution-doped samples with F_4TCNQ. Doping from vapor allows for a comparison of infiltration into as-cast and annealed films. When vapor-doping an annealed PBTTT film with F_2TCNQ, the primary absorption peak is 30% higher relative to the as-cast doped films. This difference is, in part, from the fact that annealing a neat film results in an increase in primary absorption peak by about 20% (comparison between Fig. 2, A and B). Despite the small difference in the primary absorption peak, F_2TCNQ radical anion absorption is comparable between vapor-doped films but slightly less than the solution-doped as-cast film. We attribute the higher absorption of the F_2TCNQ radical anion in solution-doped films relative to vapor-doped films to the elevated temperature of the sample during vapor deposition. In addition, the absorption curve is quantitatively similar in the NIR regime (fig. S2) for the F_2TCNQ-doped films.

Comparison of the conductivity measurements reveals that the vapor-doped PBTTT:F_2TCNQ films yield a higher σ than solution-doped films do. The annealed film has a σ of 36 ± 3 S/cm, and the as-cast film has a σ of 13.7 ± 0.2 S/cm. On the other hand, the solution-doped as-cast film has the lowest σ of 0.41 ± 0.02 S/cm despite the higher concentration of F_2TCNQ radical anion. The high vapor pressure of F_2TCNQ does not allow direct comparison of solution and vapor-doped annealed films; it leads to significant dedoping and thus several orders of magnitude lower σ of 2×10^{-3} S/cm. Nevertheless, the fact that the vapor F_2TCNQ-doped films yield higher σ further reiterates that an underlying microstructural feature is at play, which leads to a higher apparent μ.

Table 1. Summary of electronic conductivity (σ), Seebeck coefficient (α), and PF of doped PBTTT films. For the sample on an OTS-treated substrate, σ = 670 ± 4 S/cm, α = 42 ± 6 μV/K, and PF = 120 ± 30 μW m^{-1} K^{-2}. All other samples reported in this table are on untreated quartz substrates.

Dopant	Condition	σ (S/cm)	α (μV/K)	PF (μW m^{-1} K^{-2})
F_4TCNQ	Solution—as-cast	2.08 ± 0.01	45 ± 4	0.42 ± 0.09
	Solution—annealed	3.51 ± 0.05	60 ± 9	1.3 ± 0.4
	Vapor—as-cast	114.1 ± 0.5	32 ± 4	12 ± 3
	Vapor—annealed	220.00 ± 0.02	39 ± 5	32 ± 9
F_2TCNQ	Solution—as-cast	0.41 ± 0.02	111.7 ± 0.1	0.52 ± 0.03
	Solution—annealed	$2 \times 10^{-3} \pm 2 \times 10^{-4}$	755 ± 100	0.11 ± 0.03
	Vapor—as-cast	13.7 ± 0.2	130 ± 20	23 ± 6
	Vapor—annealed	36 ± 3	140 ± 20	70 ± 20

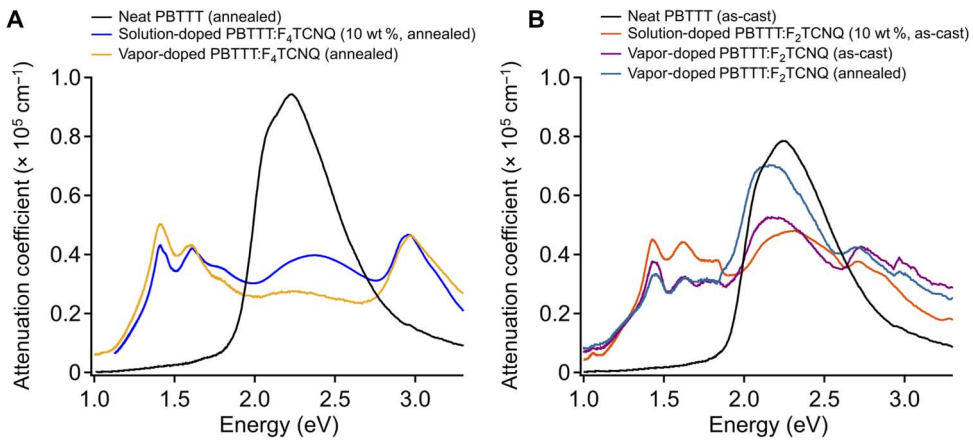

Fig. 2. UV-vis spectra of neat and doped PBTTT thin films. UV-vis spectra of (**A**) neat PBTTT and PBTTT:F_4TCNQ thin films and (**B**) PBTTT:F_2TCNQ thin films. Solution-doped films are at a dopant concentration of 10 wt %, and vapor-doped films are for dopant exposure of 10 min (all spectra normalized by thickness). Neat PBTTT films were annealed at 180°C, whereas solution-doped films were annealed at 150°C. Comparison of absorption spectra of annealed neat PBTTT and as-cast neat PBTTT can be found in the Supplementary Materials.

Processing does not change crystalline structure in doped films

To determine whether the difference in σ between vapor- and solution-doped films correlates to local structural order, we performed grazing incidence wide-angle x-ray scattering (GIWAXS) (Fig. 3). PBTTT forms semicrystalline films with strong texturing. For neat PBTTT, the out-of-plane scattering features (along the q_z axis) correspond to the lamella-stacked side chains (h00). The in-plane scattering features (along the q_{xy} axis) correspond to the (-11-3) reflection at q_{xy} = 14.2 nm^{-1} related to the chain axis and the (110) reflection at q_{xy} = 17.1 nm^{-1} associated to the π-stacking direction (*43*). The scattering pattern does not qualitatively change upon doping; that is, the features are shifted and broadened upon doping, but no new strong scattering features emerge. A significant difference between doped films and the neat film is the significant blurring of the off-axis features at q_{xy} = 14.1 nm^{-1}, suggesting disorder along the chain axis, as expected from dopants with disordered molecular orientation.

The out-of-plane scattering features of the two-dimensional (2D) GIWAXS images show changes upon doping in the alkyl side-chain stacking direction (h00) (Fig. 4A). For all doped films, we observe a small increase relative to the neat d_{100} = 2.12 nm (summarized in tables S1 and S2). Because the true out-of-plane scattering is in the inaccessible region in the grazing incidence geometry, we also obtained high-resolution specular x-ray scattering on the vapor-doped PBTTT:F_4TCNQ annealed films. The specular scattering results indicate that d_{100} = 2.37 nm, which is about a 0.25-nm increase relative to the neat film (d_{100} = 2.12 nm). In addition, the change in peak width in the (h00) direction reveals the degree of induced disorder along the side-chain stacking direction. As shown in fig. S4, the introduction of the dopant from the vapor phase introduces additional disorder relative to the neat film, which is consistent with our previous work with PBTTT:F_4TCNQ solution-doped films (*38*). Similar changes are observed for films doped with F_2TCNQ. The alkyl stacking spacing d_{100} increases by ~0.25 nm in the solution-doped PBTTT:F_2TCNQ as-cast film, whereas d_{100} increases by ~0.10 nm in the vapor-doped as-cast film and by only ~0.04 nm in the vapor-doped annealed film. This trend indicates the varying extent of dopant incorporated within the aliphatic side chains, which is consistent with the UV-vis spectra showing a slightly smaller concentration of the F_2TCNQ radical anion in vapor-doped films.

The in-plane scattering profiles along the q_{xy} axis of the 2D GIWAXS images (Fig. 4B and fig. S5) reveal that all highly doped films lead to an increase in the scattering vector for the (110) reflection (tables S1 and S2). This increase indicates a compression of the characteristic π-π–stacking distance. The value of d_{110} decreases from 0.367 nm for the neat film to 0.355 nm for the F_4TCNQ solution-doped film and 0.353 nm for the vapor-doped film. The F_2TCNQ-doped films also showed compression upon doping, where d_{110} = 0.353 nm for an as-cast solution-doped film, d_{110} = 0.357 nm for a vapor-doped as-cast film, and d_{110} = 0.361 nm for a vapor-doped annealed film. When thermal annealing a F_2TCNQ solution-doped film at 150°C, we observe rapid dedoping, where d_{110} essentially returns to the value of an annealed neat film. The vapor F_2TCNQ-doped annealed film yields the smallest decrease in d_{110}, which is consistent with the low concentration of F_2TCNQ radical anion (Fig. 2). We have previously shown that TCNQ, which does not result in an integer charge transfer with PBTTT due to the large offset between EA and IE, causes no measurable changes to the d_{110} value relative to the neat film (*38*). This result suggested that the presence of ionized polymers and dopants is partly responsible for the decrease in the characteristic d_{110} spacing. Overall, the changes to in-plane scattering features are quite similar with both doping methods.

Previously, nuclear magnetic resonance (NMR) experiments on bulk samples of PBTTT:F_4TCNQ cast from solution were carried out to determine the location of F_4TCNQ relative to the backbone of PBTTT (*38*). 2D $^{13}C\{^1H\}$ heteronuclear (HETCOR) NMR data demonstrated a very close contact between carbon atoms on the cyano group of F_4TCNQ and aromatic protons on the PBTTT backbone. This proximity and the calculated geometry for model structures of charge transfer between polymers and F_4TCNQ from density functional theory suggested that the F_4TCNQ was intercalated between the polymer backbones (*38*). Full structural modeling to compare the NMR and x-ray data was not carried out in the initial study. In contrast, a recent report on vapor-doped PBTTT:F_4TCNQ films proposed that F_4TCNQ resides in the side-chain region of PBTTT films, with the rationale that the π-stacking spacing, separation between chains, was unperturbed in their x-ray scattering data (*37*). As discussed above, we observe a compression in the π-stacking spacing relative to the neat polymer, as observed in heavily doped PBTTT films with a variety of

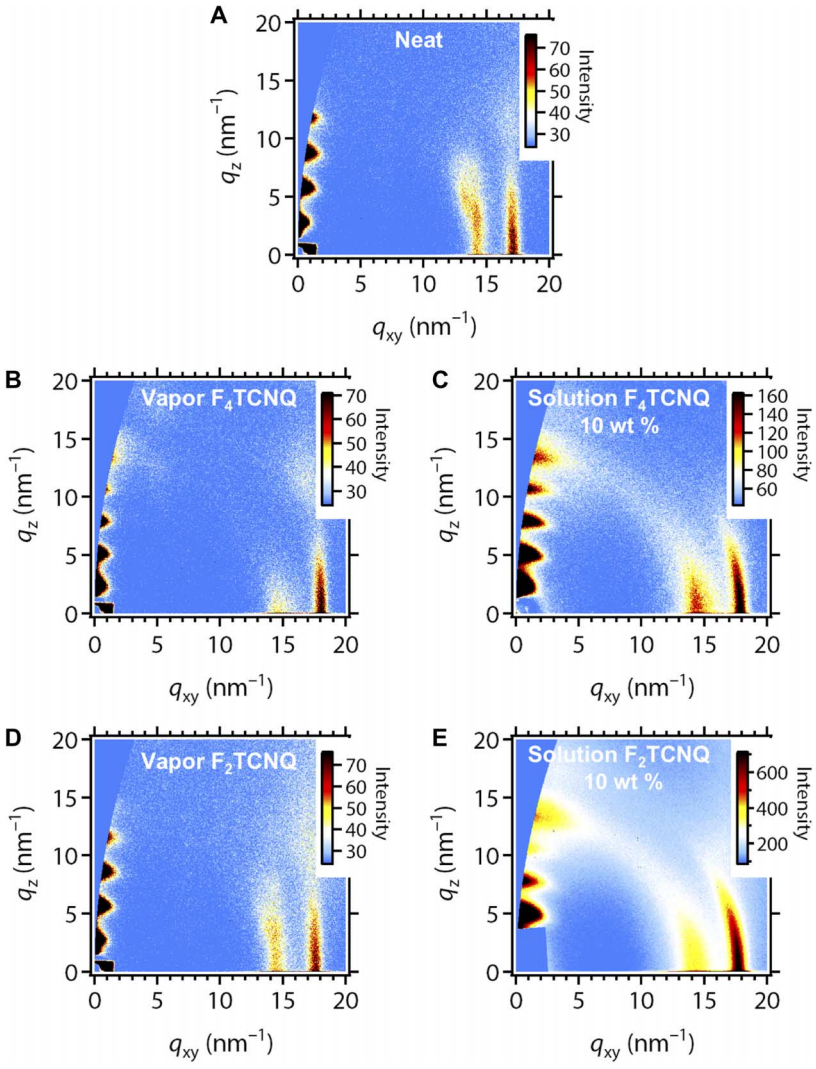

Fig. 3. GIWAXS for PBTTT films as a function of processing. 2D GIWAXS images for (**A**) annealed neat PBTTT, (**B**) F_4TCNQ vapor-doped annealed film, (**C**) annealed F_4TCNQ solution-doped film, (**D**) F_2TCNQ vapor-doped annealed film, and (**E**) as-cast F_2TCNQ solution-doped film. The (100) reflection in GIWAXS image in (E) was blocked off with lead tape to allow longer exposure time without saturating the detector. Images are obtained at Stanford Synchrotron Radiation Lightsource (SSRL) beamline 11-3.

dopants (*33*, *38*) and is reversible upon thermal removal of the dopant. Independent of these differences, one can infer that F_4TCNQ resides in the side chains for vapor-doped samples by a simple consideration. On the basis of the observed out-of-plane scattering (*h*00), we would expect <11% thickness change upon doping crystalline domains. However, for the structural model where the molecule is intercalated between in-plane π-stacked chains, we would expect a significant expansion of crystallites to compensate for the volume occupied by the dopant molecule, leading to a large in-plane expansion or significant increase in thickness to maintain the lateral size. Starting with a neat film with thickness of 25 ± 3 nm, the vapor doping process leads to a thickness of 27 ± 3 nm, which is comparable to the expected expansion of the crystallites (fig. S6). Because the film thickness does not markedly increase, F_4TCNQ resides within the aliphatic side chains (assuming a high degree of crystallinity, which is known for PBTTT). At this point, we cannot reconcile these data with the previous NMR data without detailed modeling of the spectra, which is beyond the scope of the work here. However, it is possible that the structure of the doped films has tilted PBTTT chains that allow a closer contact with the cyano groups of F_4TCNQ; such a change in tilt occurs in cocrystals of PBTTT and [6,6]-phenyl C61 butyric acid methyl ester (PCBM) (*48*).

Correlation of domain orientation controls the electrical conductivity

Small perturbations in the local structure observed by GIWAXS are similar for both solution doping and vapor doping methods and do not explain the differences in σ. Our conclusion is in contrast to the explanation of Kang *et al.* (*37*), where they attributed the higher σ only to minimal perturbation to local order. However, it is important to remember that GIWAXS only provides structural information for short-range crystalline domains (5 to 20 nm). For larger length scales, we require a small-angle scattering method. Here, we use polarized resonant soft x-ray scattering (RSoXS) that can reveal the length scale of molecular orientation in both the crystalline and amorphous domains over the range from ~10 to 1000 nm (*42*).

RSoXS leverages soft x-ray absorption to increase the scattering length and to control the scattering contrast (*42*, *49*). In π-conjugated molecules, the transition dipole moment (TDM) for the excitation

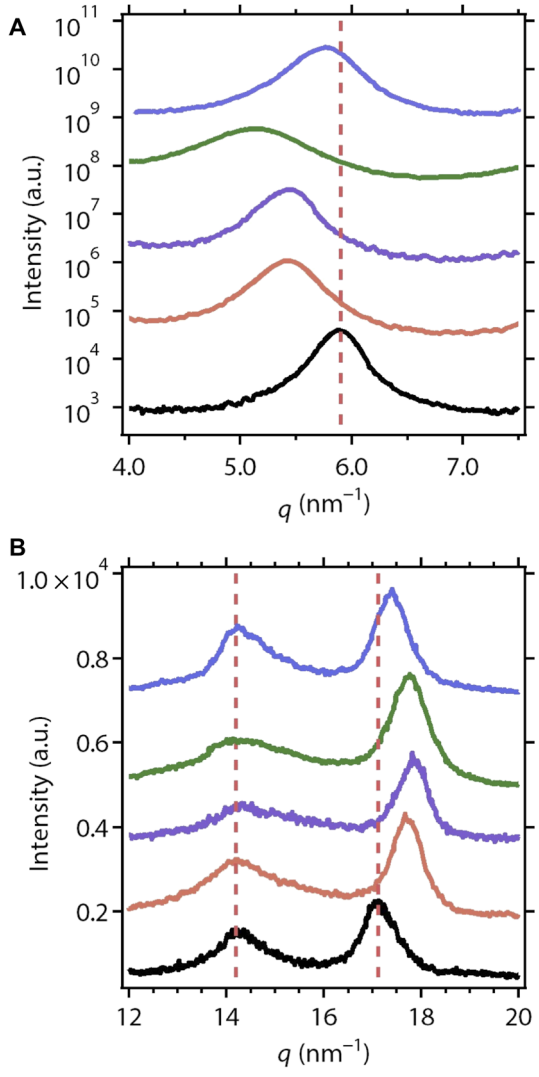

Fig. 4. Out-of-plane and in-plane scattering profiles of annealed neat and doped PBTTT thin films. GIWAXS line cuts of (**A**) out-of-plane scattering and (**B**) in-plane scattering. Black, neat; orange, F_4TCNQ solution doping; purple, F_4TCNQ vapor doping; green, F_2TCNQ solution doping; blue, F_2TCNQ vapor doping. The F_2TCNQ-doped film corresponds to as-cast conditions. Dashed red lines are guides to the eye relative to the peak positions for the neat film. All scattering profiles correspond to thermally annealed films, except for the F_2TCNQ solution doping, which is for the as-cast case. a.u., arbitrary units.

of a core electron to an unoccupied p-orbital is orthogonal to the π-conjugated plane of the molecule (*50*). By using a linearly polarized soft x-ray with the electric field vector in the plane of the film and tuning the photon energy to the C 1s to π* resonance (285.4 eV for PBTTT), scattering contrast arises from the variations in molecular orientation. For PBTTT thin films, strong resonant scattering is expected in transmission mode because the π-stacking orientation is primarily in the plane of the film (that is, TDM of the 1s to π* resonance is in the plane of film). Using RSoXS measurements, we can quantify the backbone alignment through the orientational correlation length (OCL). The OCL is defined as the average length over which the polymeric backbones (that is, the LC director) drift out of alignment with each other. The OCL was shown to have an empirical exponential relationship with field-effect μ values, providing the first direct evidence that orientational alignment of polymer backbones is the key factor influencing the performance of OTFTs (*42*).

We prepared samples to mimic, or replicate, films used for measurements of electrical conductivity. 2D RSoXS patterns were measured by transmission through polymer thin films spin-coated on top of untreated silicon nitride windows. We assume minimal difference in morphology when comparing films on silicon nitride windows and untreated quartz substrate used for conductivity measurements. On the other hand, vapor-doped PBTTT films on octadecyltrichlorosilane (OTS)–treated substrates were floated onto silicon nitride windows. All the scattering images showed a diffuse isotropic ring (fig. S7) that was azimuthally averaged to obtain a 1D scattering profile [intensity (I) versus q] (Fig. 5). The OCL is one-half of the characteristic length scale ($d^* = 2\pi/q^*$) obtained from the primary scattering peak (q^*) of the Lorentz-corrected (I^*q^2) scattering profile. The peak position was determined from fits using log-normal function. For equivalent annealing times (10 min), the OCL of neat PBTTT is sensitive to the annealing temperature above the LC transition. The OCL is ~140 and ~180 nm when annealed at 150° and 180°C, respectively (fig. S8 and table S3). Note that neat films were annealed at 180°C, whereas solution-doped films were annealed at 150°C to minimize dedoping of F_4TCNQ.

Doped films with the higher values of the OCL correlate to higher σ and, thus, higher apparent μ because of the comparable level of doping. The OCL of doped films of PBTTT depends strongly on the processing method (Fig. 5 and table S3). F_4TCNQ vapor-doped annealed films have an OCL of ~220 nm, whereas the OCL for an annealed doped film cast from solution is ~44 nm. The vapor-doped film and neat annealed PBTTT films have relatively similar OCLs. Annealed films vapor-doped with F_2TCNQ have an OCL of ~210 nm, suggesting that the introduction of the molecular dopant does not have a large impact on the OCL. The OCL of ~100 nm of solution-doped PBTTT:F_2TCNQ films after thermal annealing at 150°C for 10 min approaches the OCL of a neat film annealed at 150°C (OCL, ~140 nm) likely due to dedoping, which allows the morphology to change. Therefore, we assert that the improved orientational alignment of the backbone leads to a higher μ in vapor-doped films, similar to previous observations for OTFTs.

The trends in the OCL for as-cast doped films further confirm the significant role of backbone alignment in controlling σ. The OCL of an as-cast neat film is ~70 nm, whereas that of the as-cast film from the PBTTT:F_4TCNQ solution is ~40 nm. This difference indicates that doping in solution slightly reduces the OCL relative to a neat film before annealing. Moreover, the OCL observed for as-cast films is essentially identical to the annealed solution-doped film (OCL, ~44 nm). This similarity shows that annealing a heavily doped film has no effect on enhancing the backbone alignment, and confirms why the σ of as-cast and annealed solution-doped films is nearly identical. The fact that the OCL does not increase with annealing a solution-doped film is not surprising because the PBTTT is now heavily charged, which shifts the LC transition temperature to higher values and thus does not enter an LC mesophase when annealing at 150°C. Attempts to anneal the films at higher temperatures result in significant dedoping (*38*). For as-cast F_2TCNQ solution-doped films, we observe a qualitatively different scattering profile relative to the as-cast neat and F_4TCNQ-doped films. The scattering peaks are broader where the primary peak is at a lower $q \sim 0.03$ nm^{-1} (OCL, ~130 nm). This suggests that aggregation of PBTTT in solution, which dictates the as-cast thin film morphology, is different when using a weak molecular dopant like F_2TCNQ.

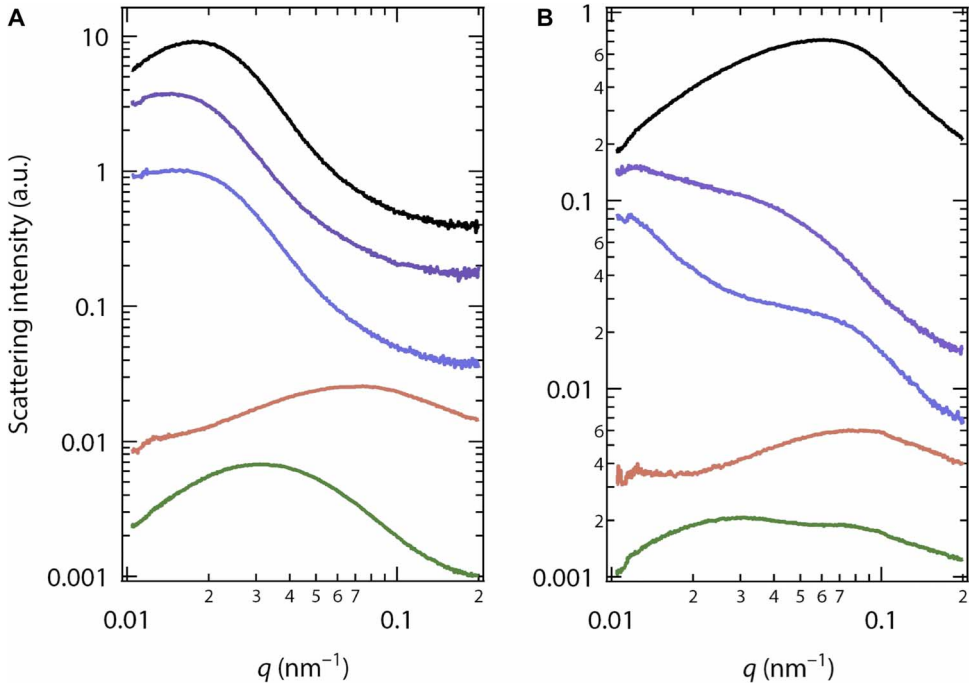

Fig. 5. RSoXS of doped films. Lorentz-corrected scattering profiles (log-log scale) from azimuthally averaged RSoXS images at a photon energy of 285.4 eV for (**A**) annealed and (**B**) as-cast films. The curves were offset for clarity. Black, neat; purple, F_4TCNQ vapor doping; blue, F_2TCNQ vapor doping; orange, F_4TCNQ solution doping; green, F_2TCNQ solution doping. RSoXS experiments were performed at Advanced Light Source (ALS) beamline 11.0.1.2.

When vapor-doping an as-cast film, we observe a qualitatively different scattering profile relative to the as-cast neat film. Essentially, two broad scattering peaks are seen around $q \sim 0.04$ nm^{-1} (OCL, ~130 nm), and another is seen at the experimental low q limit (<0.01 nm^{-1}). We see a similar effect for a F_2TCNQ vapor-doped film, where we see a peak around $q \sim 0.05$ nm^{-1} (OCL, ~60 nm) and another at experimental low q limit. The second scattering peak corresponds to an OCL that is larger than that of an as-cast neat film. The larger correlated domains provide better charge transport, leading to the high $\sigma = 114.1 \pm 0.5$ S/cm for F_4TCNQ vapor-doped as-cast films and $\sigma = 13.7 \pm 0.2$ S/cm for F_2TCNQ vapor-doped as-cast films. We can rule out that this change is due to a thermal annealing process; the sample underneath the lid is calibrated to be approximately 85°C, which is well below the LC transition temperature and has no effect on the OCL (fig. S8 and table S3).

Increasing electrical conductivity through processing

Comparison of σ and the OCL reveals that long backbone correlation lengths allow for more efficient charge transport. It has been previously shown that the OCL of PBTTT can be controlled depending on the polarity of the substrate surface (*42*). In particular, substrates functionalized with a nonpolar monolayer of OTS lead to the largest OCL of ~380 nm for an annealed neat PBTTT thin film (*42*). Vapor-doping a PBTTT thin film annealed on an OTS-functionalized substrate with F_4TCNQ yielded a σ of 670 ± 4 S/cm. This σ is a factor of ~3 higher value than the vapor-doped film on a bare substrate. The corresponding OCL is also higher at ~350 nm (versus 210 nm for the doped film on a bare substrate). UV-vis-NIR absorption measurements (fig. S3) confirm that the doping level is similar for both cases. Therefore, the increase in σ is entirely from a higher apparent μ and reiterates the significance of the OCL as a parameter to describe the trends in σ.

A significant assumption in previous work on the relationship between the μ from OTFTs and the OCL was that the OCL, a bulk property, correlates to an interface-dominated charge transport measurement. Here, we can eliminate that assumption because σ is a bulk transport property, and conclusively show the correlation between OCL and σ and, thus, apparent μ. To determine the sensitivity of σ to the OCL, we plot log(σ) versus OCL for various doped films in Fig. 6A. The increase in σ is most significant at lower OCL values and then approaches a plateau at higher OCL values. The data points in Fig. 6A are at comparable doping levels with respect to F_4TCNQ samples, thus indicating that the apparent μ is the parameter increasing with OCL. The correlation of the interfacial mobility from OTFTs and that from the bulk conductivity likely holds in PBTTT because GIWAXS typically shows highly oriented crystallites with a thickness equivalent to the total film. In materials where the interfacial and bulk structures are dissimilar, we might not expect such a relationship to hold.

Extrapolation of σ to higher OCL values using Fig. 6A provides valuable information on the limits of electrical performance. The chain alignment process effectively increases the OCL, where an infinite OCL corresponds to perfect alignment. When approaching the limit of an infinite OCL, one would expect σ to plateau as the net increase in μ becomes smaller (*51*). For comparison, the mobility in OTFTs of PBTTT thin films prepared on an OTS-treated substrate and subsequently strained aligned has been measured (*52*). The alignment process resulted in a factor of ~2 increase in μ according to field-effect transistor measurements (*52*). This observation suggests that σ could increase to ~1300 S/cm relative to our highest-performing PBTTT: F_4TCNQ vapor-doped film if the bulk and interfacial mobilities remain correlated.

The determination of the connection between the OCL and σ shows the significance of processing on the transport properties of

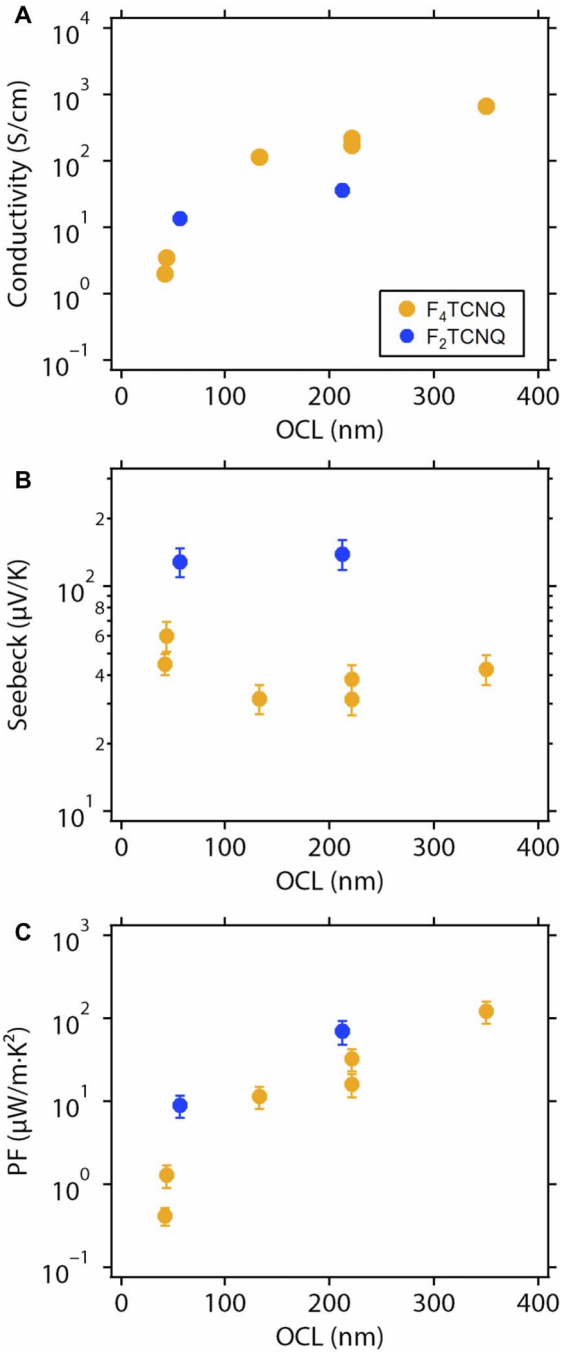

Fig. 6. The relationship between OCL and thermoelectric material properties. (**A**) Measured electronic conductivity (σ), (**B**) measured Seebeck coefficient (α), and (**C**) calculated PF versus the corresponding OCL values, as determined from the RSoXS experiments (table S3).

doped semiconducting polymers. Although the vapor doping process yields the highest values of σ here, the vapor doping process with F_4TCNQ is not the only method to achieve high σ. In our previous work, doping annealed films of PBTTT through exposure to a vapor of a fluorinated trichlorosilane (FTS) or immersion in a 4-ethylbenzene sulfonic acid solution yielded σ of around 1000 S. The likely origin is that the OCL was set before doping and not substantially perturbed by the doping process. It is difficult to directly compare the conductivities of the two studies because of the question of the carrier concentration with different dopants. One can also imagine achieving high σ when casting films from a polymer/dopant solution if the processing steps lead to a solid-state thin film with a large OCL.

Comparison to previous work reported in the literature further reiterates the critical role of controlling the morphology to achieve efficient charge transport. Sequential doping of P3HT with F_4TCNQ results in films with higher σ relative to solution-doped films (*35*), which is driven by improved interconnectivity between ordered π-stacked domains (*36*). Sequentially doping P3HT with F_4TCNQ in nonpolar solvents yields a larger 5 to 10 factor increase in σ (*36*). These films also have good interconnectivity, but phase segregation of dopants in the disordered domains was suggested as the reason for the higher σ. Other factors such as the molecular structure of the dopant and its solubility in the polymer can also influence morphology and thus σ (*26*). Polar side chains on polymers have been found to increase the thermal stability of F_4TCNQ-doped films, which is particularly useful for thermoelectric energy conversion (*53*). The environmental stability of F_4TCNQ in thiophene-based polymers is a concern due to photochemical reactions, which will require investigation into appropriate encapsulation for devices (*53*–*55*).

Role of morphology on Seebeck coefficient and PF

Although the impact of the orientation of domains on σ is relatively straightforward to understand, the impact on α is less clear. Unlike σ, which describes the transport of charge carriers relative to an electric field, α describes the migration of charge carriers relative to temperature gradient at the open circuit condition. This is quantified by measuring the voltage drop (ΔV) relative to temperature difference (ΔT). Fundamentally, α is related to the population in the electronic DOSs of a material and carrier scattering processes. The expression for the thermopower as a function of electronic conductivity function σ(E) is given as

$$\alpha = \frac{k_B}{e}\int \frac{(E - E_F)}{k_b T}\frac{\sigma(E)}{\sigma}\frac{\partial f(E)}{\partial E}\,dE \quad (1)$$

where E_F is the Fermi energy, σ is the total conductivity, $f(E)$ is the Fermi function, and k_B/e is a natural unit of thermopower of 86.17 μV/K (*56*). As the semiconductor is p-doped, the Fermi level shifts closer to the valence band, which results in a decrease in the value of α. The introduction of a molecular dopant into a polymer will also modify the local structure and morphology, making it difficult to model the thermoelectric properties with a constant electronic DOS. There have been significant efforts to model the thermoelectric properties of polymers (*56*–*58*), but these models do not, as yet, consider morphology.

The overall thermoelectric properties of PBTTT depend strongly on processing methods (Table 1). For example, α = 60 ± 9 and PF = 1.3 ± 0.4 μW m^{-1} K^{-2} for the solution-doped annealed film of PBTTT:F_4TCNQ, whereas annealing followed by vapor infiltration of F_4TCNQ leads to α = 39 ± 5 μV/K and PF = 32 ± 9 μW m^{-1} K^{-2} (Table 1). Despite the lower α, PF is higher for vapor-doped films due to the nearly 100-fold increase in σ. The difference in α with vapor doping can be attributed, in part, to the slightly higher concentration of F_4TCNQ based on the UV-vis spectra, but the morphology of these two films is also quite different. Furthermore, α = 42 ± 6 μV/K for the F_4TCNQ vapor-doped film on an OTS-treated substrate, which indicates that α is less sensitive to the substrate treatment than

σ. However, the near factor of 3 increase in σ results in the high PF of 120 ± 30 μW m^{-1} K^{-2}.

With F_2TCNQ as the dopant, we observe α values of 111.7 ± 0.1 μV/K for the as-cast solution-doped film, 130 ± 20 μV/K for the vapor-doped as-cast film, and 140 ± 20 μV/K for the vapor-doped annealed film (Table 1). The higher α relative to F_4TCNQ is not surprising because of the likely lower concentration of F_2TCNQ in the film and potentially lower efficiency of carrier formation. The F_2TCNQ vapor-doped annealed film yields the highest α, consistent with the slightly lower doping efficiency, as indicated by UV-vis (Fig. 2). Owing to the high σ of 36 ± 3 S/cm, the corresponding PF is 70 ± 20 μW m^{-1} K^{-2}. Despite the lower σ relative to the F_4TCNQ vapor-doped film on a bare quartz substrate, the PF is greater because of the large α value. This shows the importance of tuning α while not significantly sacrificing σ.

Comparison of α to the corresponding OCL reveals that, unlike σ, the value of α does not show marked changes (Fig. 6B). For F_4TCNQ-doped samples, α is in the range of 30 to 60 μV/K for the full OCL window. In addition, the F_2TCNQ samples are essentially the same (~130 μV/K) at different OCL values. There appears to be a small upward trend for vapor-doped samples, but overall α is less sensitive to polymer chain alignment. Some recent work on the anisotropy of σ and α on PEDOT:PSS [poly(3,4-ethylenedioxythiophene)-poly(styrenesulfonate)] films (*59*) and P3HT films (*60*) also suggests that α is relatively unaffected by polymer chain alignment, and thus, changes in PF with the OCL (Fig. 6C) are dominated by the increase in σ. This observation would be expected if the shape of the electronic DOS was relatively constant and the number of carriers was similar, that is, no large change in the Fermi level. Temperature-dependent α and σ measurements are needed to fully elucidate the transport mechanism from both doping processes.

Previously, we determined an empirical correlation where α follows a power-law dependence with σ ($\alpha \propto \sigma^{-1/4}$) and PF follows a square root dependence with σ ($PF \propto \sigma^{1/2}$) for a variety of p-doped thiophene-based polymers. This correlation was primarily determined on solution-doped films and thermal annealing conditions 150°C or below. In Fig. 7 , we plot the empirical correlations (dashed lines) along with α and PF values reported in this study. The solution-doped samples follow the empirical trends. On the other hand, vapor-doped samples deviate from the empirical trends, where the values are observed to be higher than expected at corresponding σ values. The positive deviation of α and PF relative to the empirical trend line is most pronounced for vapor-doped PBTTT:F_4TCNQ and also for both solution- and vapor-doped PBTTT:F_2TCNQ films. The PF of our highest-performing PBTTT:F_4TCNQ film is similar to our previous work on PBTTT vapor-doped with an interfacial FTS (green diamond marker in Fig. 7) (*33*). It has recently been proposed that the power-law relationship is due to a change in the energy-dependent conductivity function of the material [σ(*E*)] (*56*). The higher PF here would suggest that this function is affected by processing conditions speculated in that work.

Future routes to improve the PF of polymers

Although we have focused only at the limit of high doping level, systematically varying the doping level and the OCL provides a route to optimization of the PF. We can also consider the performance of PEDOT, which has been the benchmark conducting polymer for thermoelectrics (*7*). A PF as high as ~460 μW m^{-1} K^{-2} has been reported (*61*), and σ of ~5000 S/cm has been measured for metallic template polymerized PEDOT doped with sulfuric acid (*62*). This σ is comparable to the performance of polyacetylene (~10^5 S/cm) (*63*). A question is whether the higher conductivities of these materials are due to the electronic structure of the conjugated backbone or other factors. In comparison to these materials, the presence of alkyl side chains on semiconducting polymers, such as PBTTT, results in a significant volume of the material being insulating. Accounting for the insulating side chains reveals an effective electronic conductivity (σ_{eff}) of the conjugated core representing densely packed polymer chains (*37*). For PBTTT with tetradecyl side chains, the conjugated core accounts for approximately 15% of the volume in a film (determined from the unit cell of PBTTT). The σ_{eff} would translate to ~4000 S/cm for our highest-performing film. If these structural changes can be achieved without changing the α, the PF could reach values of ~500 μW m^{-1} K^{-2} at high levels of doping similar to PEDOT. Removal, or shortening, of the side chains of a polymer leads to difficulties in processing, that is, PEDOT is poorly soluble and is cast as a dispersion or directly grown on a substrate. The dopant itself also modifies the volume of the doped material. However, this comparison shows that conjugated backbones other than PEDOT have significant promise if their structure can be judiciously modified to maintain their processability and allow for incorporation of the dopant.

Potential impact of processing on thermal conductivity

Our study reveals the potential benefits that local chain alignment can play in further improving PF, but one should also consider the impact on *ZT*. Changes in the OCL likely modify the thermal conductivity (κ) through both the phonon (lattice) contribution (κ_L) (*64*) and, at sufficiently high *n* and σ, the electronic contribution to thermal conductivity (κ_e). Note that experimental challenges still remain on the determination of κ of thin films and particularly along the in-plane direction (*6*). Techniques such as suspended microdevices (*65*) or the membrane-based ac calorimetry (*66*) can help to determine the in-plane κ. The membrane-based ac calorimetry method revealed an in-plane κ of 0.39 W m^{-1} K^{-1} for an as-cast neat PBTTT film (1 μm thick) (*66*). Films with high σ, for example, F_4TCNQ-doped film at 640 S/cm, could result in a significant contribution from κ_e. PEDOT:PSS, for example, has a significant contribution from κ_e at a σ of ~500 S/cm and higher (*67*). Therefore, there may be an optimization process on the extent of alignment and doping level that leads to a minimal increase of κ to achieve a high *ZT*. A potential optimization process can be seen through the example of PBTTT:F_2TCNQ, which yields lower σ of 36 S/cm relative to PBTTT:F_4TCNQ (220 S/cm) at a comparable OCL value of ~200 nm (Fig. 5A). Despite the lower σ, the PBTTT:F_2TCNQ film yields a higher α and thus a larger PF of 70 μW m^{-1} K^{-2} relative to the PBTTT:F_4TCNQ film (PF = 32 μW m^{-1} K^{-2}) (Fig. 5, B and C). As a consequence, the lower σ can be leveraged to minimize, in principle, the electronic contributions to κ while still being able to achieve a relatively high PF.

Summary

We have explored how solution- and vapor-doping a high-mobility p-type polymer, PBTTT-C_{14}, affect its thermoelectric transport properties and its underlying microstructure. Overall, vapor-doping with either F_4TCNQ or F_2TCNQ yields higher σ relative to solution-doped films. The enhancement in σ is not related to the local order because the perturbations to the local structure are minimal and similar with either doping route. We determined using RSoXS that the alignment of ordered domains, quantified through the OCL, is a critical parameter in explaining trends in σ. The larger OCL for vapor-doped films allows

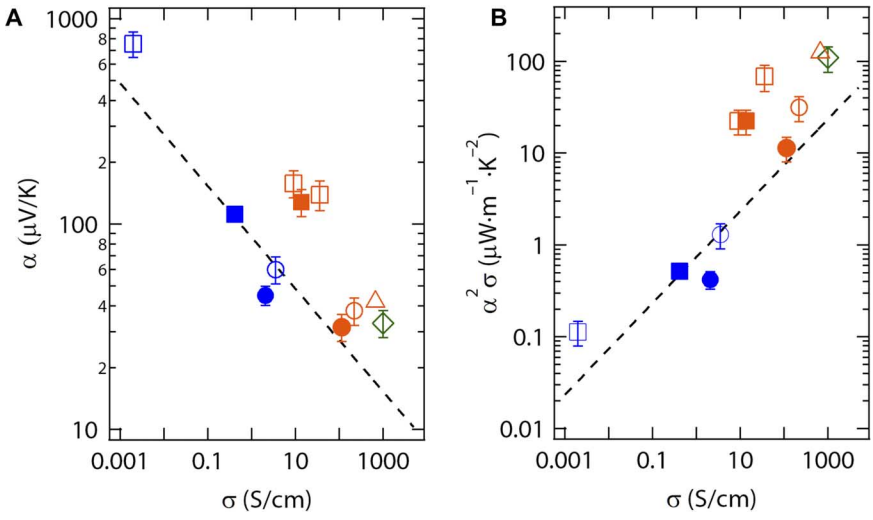

Fig. 7. Trends in Seebeck coefficient and power factor. Log-log scale plot showing the trends in (**A**) Seebeck coefficient (α) and (**B**) PF ($\alpha^2\sigma$) versus electronic conductivity (σ) for solution- and vapor-doped films. Orange markers are for vapor-doped films, and blue markers are for solution-doped films. Circle markers are for F_4TCNQ-doped films, square markers are for F_2TCNQ-doped films, and triangle marker is for the F_4TCNQ-doped film on OTS-treated substrate. Open markers correspond to thermally annealed films, and filled markers correspond to as-cast films. The open green diamond is our previously reported FTS-doped PBTTT thin film (*33*). Dashed lines are empirical trends [$\alpha \propto \sigma^{-1/4}$ and PF $\propto \sigma^{1/2}$] we previously reported on various doped semiconducting polymers (*34*).

for efficient charge transport and thus a higher σ relative to solution-doped films, which yield a smaller OCL. Owing to better long-range correlation length of backbones, a F_4TCNQ vapor-doped PBTTT-C_{14} casted on an OTS-treated substrate yields a high σ of 670 ± 4 S/cm and corresponding large α of 42 ± 6 μV/K. This translates to a PF of 120 ± 30 μW m^{-1} K^{-2}—the highest reported value for F_4TCNQ-doped semiconducting polymers. In addition, using a weaker molecular dopant like F_2TCNQ can lead to a large α (140 ± 20 μV/K) while not significantly sacrificing σ (36 ± 3 S/cm), and thus yield a large PF of 70 ± 20 μW m^{-1} K^{-2}.

With a better understanding of processing effects on σ and α, we can now outline some general processing guidelines to achieve high thermoelectric PF. First, casting a neat semiconducting polymer film that forms locally π-stacked domains with long-range correlation lengths of the conjugated backbones provides an ideal microstructure for efficient charge transport for high apparent μ. Second, introducing the molecular dopant into the polymer film (that is, from the vapor phase) to increase *n*, and in turn σ, should lead to minimal perturbation to the local order while maintaining, or enhancing, the long-range correlation lengths of conjugated backbones. By leveraging the high apparent μ and then precisely controlling the dopant concentration, or by choosing a weaker molecular dopant, one can obtain a large α while not significantly sacrificing σ. Overall, developing better doping routes and advancing our fundamental understanding of structure-property relationships of semiconducting polymers will have far-reaching implications on the deployment of lightweight and low-cost organic thermoelectric modules for thermal energy conversion and management.

MATERIALS AND METHODS

Materials

Anhydrous chlorobenzene (CB) and *o*-dichlorobenzene (ODCB) were purchased from Sigma-Aldrich. F_4TCNQ and F_2TCNQ were purchased from TCI Chemicals. OTS was purchased from Gelest. All chemicals were used as received. PBTTT-C_{14} was synthesized using literature procedure (*68*) with a number-average molecular weight (M_n) of 18,000 or 24,000 g/mol.

Neat PBTTT and PBTTT:F_nTCNQ (*n* = 2 or 4) thin-film sample fabrication

Neat PBTTT solution preparation

Neat PBTTT solutions at 5 mg/ml were prepared by dissolving PBTTT in either CB or 1:1 CB:ODCB and heated to 120°C. Approximately 1 hour was needed to fully dissolved PBTTT. The heated neat PBTTT solution was filtered using 0.45-μm polytetrafluoroethylene (PTFE) syringe filter. The PBTTT solution gels when cooled below 80°C. As a consequence, the neat PBTTT solution was maintained at 120°C before doping or spin coating.

*Solution doping of PBTTT with F_nTCNQ (*n* = 2 or 4)*

F_nTCNQ (3 wt %; *n* = 2 or 4) solution was prepared by dissolving the dopant in ODCB and heated to 150°C. To achieve 10 wt % dopant concentration, an aliquot of F_nTCNQ solution was added to the neat PBTTT solution and heated to 120°C. After the addition of the dopant, the heated polymer solution became more viscous and immediately transitioned from a red to black color. These changes were indicative of charge transfer between the polymer and dopant in solution. To minimize gelation and precipitation of the charged polymer, the PBTTT:F_nTCNQ (*n* = 2 or 4) solution was maintained at 120°C before spin coating.

Substrates

Thin films were prepared on quartz substrates (1.5 cm × 1.5 cm; University Wafers) for conductivity and Seebeck measurements, native oxide silicon substrates (1.5 cm × 1.5 cm; International Wafer Services) for GIWAXS experiments, and silicon nitride windows (window size, 1.5 mm × 1.5 mm; window thickness, 100 nm; frame size, 5 mm × 5 mm; thick frame, 200 μm; NX5150C, Norcada Inc.) for RSoXS experiments. The quartz and silicon substrates were cleaned by sonicating first in acetone and then in isopropanol. Samples of PBTTT thin films on

OTS-treated substrates were prepared by plasma-treating a quartz substrate with air for 2 min. Then, the substrate was immersed in OTS and anhydrous toluene (volume ratio, 0.10 to 1) for 10 min, heated to 80°C, and subsequently rinsed with toluene to achieve an OTS self-assembled monolayer. The OTS-treated quartz substrates were heated to 80°C in a N_2 glove box to remove the residual solvent.

Spin-coating conditions

Neat PBTTT thins films were spin-coated from a CB solution (5 mg/ml) or from a 1:1 CB:ODCB solution (5 mg/ml). The heated solution (120°C) was spin-coated first at 1000 rpm for 45 s and then at 3000 rpm for 15 s under ambient conditions. The heated (120°C) PBTTT:F_nTCNQ solution was spin-coated at 1000 rpm for 45 s and then at 3000 rpm for 15 s, which leads to the macroscopically uniform thin films with thicknesses in the range of 40 to 60 nm.

Thermal annealing

The neat PBTTT thin films were annealed in a N_2-filled glove box for 10 min at 180°C and then slowly cooled to 80°C. The thermal annealing conditions for solution-doped films were at 150°C for 10 min in a N_2-filled glove box. The thickness of the annealed film was approximately in the range of 15 to 40 nm according to atomic force microscopy (AFM; Asylum MFP-3D) measurements.

Vapor-doping process

Neat PBTTT thin films were first fabricated using the procedure outlined above. Subsequently, an as-cast or thermal annealed neat film was vapor-doped with F_nTCNQ (n = 2 or 4) in a N_2 glove box. Approximately 5 to 10 mg of dopant were placed in a glass jar (Qorpak with a PTFE lined cap; diameter, ~5 cm; height, ~4.5 cm). The polymer sample was placed underneath the cap (near the center) using double-sided tape. The closed jar was heated on a hotplate set to ~210°C. The typical heating times were in the range of 2 to 10 min. This heating process leads to a partial vapor pressure of the dopant in the jar. Successful doping of a PBTTT thin film was confirmed when the film has a nearly transparent appearance (typically achieved after 5 to 10 min for 25-nm PBTTT thin film). Successful doping was confirmed through UV-vis-NIR measurements. The temperature of a sample underneath the cap was measured using a thermocouple while the jar was heated. The sample was around 75°C after 5 min and equilibrates to around 95°C after 30 min.

UV-vis-NIR spectroscopy

UV-vis-NIR spectra of thin films on 0.5-mm-thick quartz substrates (1.5 cm × 1.5 cm) were obtained using the Shimadzu UV-3600 UV-Nir-NIR Spectrometer at the UC (University of California) Santa Barbara Materials Research Laboratory TEMPO Facility. The doped films were placed in a custom-built airtight holder to ensure doping stability. Measurements were taken within a wavelength (λ) range of 300 to 2300 nm.

Conductivity and Seebeck measurements

Gold contact layers (~100 nm thick) for electronic conductivity and Seebeck coefficient measurements were thermally evaporated (Angstrom Engineering Amod) onto either neat PBTTT thin films or solution-doped PBTTT:F_nTCNQ (n = 2 or 4) thin films through a shadow mask. Four-point probe conductivity contacts had a channel length of 0.2 mm and a channel width of 1 mm. Seebeck measurement contacts consisted of 1-mm^2 gold pads adjacent to 0.2-mm × 1-mm gold bars. The distance between the gold pads (temperature probes) and gold bars (voltage probes) was 3, 4, and 5 mm apart. A detailed schematic is provided in fig. S9.

Four-point probe conductivity measurements were performed using a custom-designed probe station in a N_2 glove box. Voltage and current measurements were performed using a Keithley 2400 source measure unit and Keithley 6221 precision current source. A constant current was applied to the outer contacts, and the resultant steady-state voltage response was recorded from the inside contacts. The resistance (R; ohms) of the sample was extracted from the slope of the VI sweep using Ohm's law ($V = IR$).

The Seebeck coefficient (α) measurements were performed in a N_2 glove box using a custom-built setup. A detailed description of the Seebeck coefficient measurement setup can be found in the study of Glaudell *et al.* (*34*). Peltier elements 5 mm apart provided the temperature difference ($\Delta T = T_H - T_C$). A minimal amount of thermal conductive paste was applied to the tips of the thermal couple to ensure good thermal contact between the thermocouple and the gold pads. The measurement system has systematic error of 15% due to thermal anchoring issues. A delay of 100 s was used for voltage measurements to ensure that a steady-state temperature gradient was reached. The Seebeck coefficient was calculated from the slope of a linear fit for the ΔV versus ΔT plot. The measurements were taken within an approximate ΔT of ±3 K around 300 K.

To infer the apparent charge carrier mobility (μ), we used the MR (dopant/monomer) values of the vapor- and solution-doped films and assumed that the dopants are fully ionized and all the hole carriers generated contribute to conductivity. Knowing the unit cell of PBTTT, we can calculate the carrier concentration (n). After which, we can calculate the mobility using the equation $\mu = \sigma/(qn)$, where σ is the electronic conductivity and q is the charge (+1).

Synchrotron x-ray scattering

2D GIWAXS images were obtained using beamline 11-3 at SSRL located on the SLAC (Stanford Linear Accelerator Center) National Accelerator Laboratory campus. Thin-film samples for GIWAXS experiments were prepared following the procedures outlined above. The samples were exposed to x-rays with a wavelength of 0.9752 Å, and 2D scattering images were obtained using a MAR345 image plate detector or MarCCD detector, which was placed 400 mm from the sample. A LaB_6 sample was used as a standard for calibration. All samples were placed in a He-filled chamber to reduce air scattering and minimize beam damage to the sample. The reported GIWAXS images were taken at a grazing incident x-ray angle of 0.10 or 0.12, which is above the critical angle of the polymer film and below the critical angle of the silicon substrate.

X-ray specular scattering was collected on beamline 2-1 using the setup with Soller slits and a photomultiplier tube. The incident x-ray energy was 11.5 keV.

RSoXS samples were prepared by directly spin-coating onto the silicon nitride windows following thin-film fabrication process outlined above. RSoXS samples from doped PBTTT thin films on an OTS-treated quartz substrate were prepared by first scribing small square grids using a razor blade. A solution of 15% hydrogen fluoride in deionized water was used to partially etch the oxide layer. The films were then lifted off the substrate by dipping them in deionized water. The pieces of freestanding films were then lifted out of the water using silicon nitride windows.

RSoXS experiments were performed on beamline 11.0.1.2 at the ALS located on the Lawrence Berkeley National Laboratory campus. 2D RSoXS scattering images were collected in transmission mode using a charge-coupled device camera (Princeton Instrument PI-MTE)

cooled to −45°C in a high-vacuum chamber (add pressure). The sample-to-detector distance was set to 175 mm. The 2D scattering image was reduced by azimuthal integration over all values of q (scattering vector). After subtraction of the dark image, the Lorentz-corrected profile (I^*q^2 versus q) was obtained. The data reduction was performed in Wavemetrics Igor Pro using NIKA macro developed by J. Ilvasky at the Advanced Photon Source (*69*).

SUPPLEMENTARY MATERIALS

Supplementary material for this article is available at http://advances.sciencemag.org/cgi/content/full/3/6/e1700434/DC1

fig. S1. AFM height and phase images of neat annealed PBTTT and F_4TCNQ vapor-doped films at 5 and 10 min.

fig. S2. Absorption spectra showing the NIR regime for doped PBTTT films and the thermal stability of F_2TCNQ-doped films.

fig. S3. Additional UV-vis-NIR spectra of F_4TCNQ vapor-doped films relative to a neat film.

fig. S4. Williamson-Hall plot for neat (black circle) and F_4TCNQ vapor-doped film.

fig. S5. In-plane scattering profiles of as-cast neat and doped films.

fig. S6. Thin-film thickness profile of neat and vapor-doped PBTTT:F_4TCNQ film.

fig. S7. Representative 2D RSoXS images for neat PBTTT, F_4TCNQ vapor-doped, and F_4TCNQ solution-doped thin films (all thermally annealed).

fig. S8. Lorentz-corrected scattering profiles of neat PBTTT for different annealing temperatures.

fig. S9. Schematic of the geometry of the contacts for electronic conductivity and Seebeck measurements on thin films of doped polymers.

table S1. X-ray reflection peaks of annealed PBTTT thin films from GIWAXS.

table S2. X-ray reflection peaks of as-cast PBTTT thin films from GIWAXS.

table S3. Summary of OCLs for doped films.

REFERENCES AND NOTES

1. B. Lüssem, M. Riede, K. Leo, Doping of organic semiconductors. *Phys. Status Solidi A* **210**, 9–43 (2013).
2. H. Ma, H.-L. Yip, F. Huang, A. K.-Y. Jen, Interface engineering for organic electronics. *Adv. Funct. Mater.* **20**, 1371–1388 (2010).
3. M.-C. Jung, S. R. Raga, L. K. Ono, Y. Qi, Substantial improvement of perovskite solar cells stability by pinhole-free hole transport layer with doping engineering. *Sci. Rep.* **5**, 9863 (2015).
4. G. Lu, J. Blakesley, S. Himmelberger, P. Pingel, J. Frisch, I. Lieberwirth, I. Salzmann, M. Oehzelt, R. Di Pietro, A. Salleo, N. Koch, D. Neher, Moderate doping leads to high performance of semiconductor/insulator polymer blend transistors. *Nat. Commun.* **4**, 1588 (2013).
5. O. Bubnova, X. Crispin, Towards polymer-based organic thermoelectric generators. *Energy Environ. Sci.* **5**, 9345–9362 (2012).
6. S. N. Patel, M. L. Chabinyc, Anisotropies and thermoelectric properties of semiconducting polymers. *J. Appl. Polym. Sci.* **134**, 44403 (2016).
7. B. Russ, A. Glaudell, J. J. Urban, M. L. Chabinyc, R. A. Segalman, Organic thermoelectric materials for energy harvesting and temperature control. *Nat. Rev. Mater.* **1**, 16050 (2016).
8. O. Owoyele, S. Ferguson, B. T. O'Connor, Performance analysis of a thermoelectric cooler with a corrugated architecture. *Appl. Energy* **147**, 184–191 (2015).
9. Q. Wei, M. Mukaida, K. Kirihara, Y. Naitoh, T. Ishida, Polymer thermoelectric modules screen-printed on paper. *RSC Adv.* **4**, 28802 (2014).
10. J.-H. Bahk, H. Fang, K. Yazawa, A. Shakouri, Flexible thermoelectric materials and device optimization for wearable energy harvesting. *J. Mater. Chem. C* **3**, 10362–10374 (2015).
11. C. Wan, R. Tian, A. B. Azizi, Y. Huang, Q. Wei, R. Sasai, S. Wasusate, T. Ishida, K. Koumoto, Flexible thermoelectric foil for wearable energy harvesting. *Nano Energy* **30**, 840–845 (2016).
12. H. Fang, B. C. Popere, E. M. Thomas, C.-K. Mai, W. B. Chang, G. C. Bazan, M. L. Chabinyc, R. A. Segalman, Large-scale integration of flexible materials into rolled and corrugated thermoelectric modules. *J. Appl. Polym. Sci.* **134**, 44208 (2017).
13. K. Kirihara, Q. Wei, M. Mukaida, T. Ishida, Thermoelectric power generation using nonwoven fabric module impregnated with conducting polymer PEDOT:PSS. *Synth. Met.* **225**, 41–48 (2017).
14. G. J. Snyder, E. S. Toberer, Complex thermoelectric materials. *Nat. Mater.* **7**, 105–114 (2008).
15. A. Salleo, R. J. Kline, D. M. DeLongchamp, M. L. Chabinyc, Microstructural characterization and charge transport in thin films of conjugated polymers. *Adv. Mater.* **22**, 3812–3838 (2010).
16. P. Pingel, D. Neher, Comprehensive picture of *p*-type doping of P3HT with the molecular acceptor F_4TCNQ. *Phys. Rev. B* **87**, 115209 (2013).
17. V. I. Arkhipov, P. Heremans, E. V. Emelianova, G. J. Adriaenssens, H. Bässler, Charge carrier mobility in doped semiconducting polymers. *Appl. Phys. Lett.* **82**, 3245–3247 (2003).
18. V. I. Arkhipov, E. V. Emelianova, P. Heremans, H. Bässler, Analytic model of carrier mobility in doped disordered organic semiconductors. *Phys. Rev. B* **72**, 235202 (2005).
19. B. Lüssem, C.-M. Keum, D. Kasemann, B. Naab, Z. Bao, K. Leo, Doped organic transistors. *Chem. Rev.* **116**, 13714–13751 (2016).
20. H. Sirringhaus, 25th anniversary article: Organic field-effect transistors: The path beyond amorphous silicon. *Adv. Mater.* **26**, 1319–1335 (2014).
21. R. Noriega, J. Rivnay, K. Vandewal, F. P. V. Koch, N. Stingelin, P. Smith, M. F. Toney, A. Salleo, A general relationship between disorder, aggregation and charge transport in conjugated polymers. *Nat. Mater.* **12**, 1038–1044 (2013).
22. D. Venkateshvaran, M. Nikolka, A. Sadhanala, V. Lemaur, M. Zelazny, M. Kepa, M. Hurhangee, A. J. Kronemeijer, V. Pecunia, I. Nasrallah, I. Romanov, K. Broch, I. McCulloch, D. Emin, Y. Olivier, J. Cornil, D. Beljonne, H. Sirringhaus, Approaching disorder-free transport in high-mobility conjugated polymers. *Nature* **515**, 384–388 (2014).
23. J. B. Torrance, An overview of organic charge-transfer solids: Insulators, metals, and the neutral-ionic transition. *Mol. Cryst. Liq. Cryst.* **126**, 55–67 (1985).
24. K.-H. Yim, G. L. Whiting, C. E. Murphy, J. J. M. Halls, J. H. Burroughes, R. H. Friend, J.-S. Kim, Controlling electrical properties of conjugated polymers via a solution-based p-type doping. *Adv. Mater.* **20**, 3319–3324 (2008).
25. C. Wang, D. T. Duong, K. Vandewal, J. Rivnay, A. Salleo, Optical measurement of doping efficiency in poly(3-hexylthiophene) solutions and thin films. *Phys. Rev. B* **91**, 85205 (2015).
26. J. Li, G. Zhang, D. M. Holm, I. E. Jacobs, B. Yin, P. Stroeve, M. Mascal, A. J. Moulé, Introducing solubility control for improved organic p-type dopants. *Chem. Mater.* **27**, 5765–5774 (2015).
27. J. B. Torrance, The difference between metallic and insulating salts of tetracyanoquinodimethone (TCNQ): How to design an organic metal. *Acc. Chem. Res.* **12**, 79–86 (1979).
28. F. Wudl, From organic metals to superconductors: Managing conduction electrons in organic solids. *Acc. Chem. Res.* **17**, 227–232 (1984).
29. M. R. Bryce, L. C. Murphy, Organic metals. *Nature* **309**, 119–126 (1984).
30. P. Pingel, R. Schwarzl, D. Neher, Effect of molecular p-doping on hole density and mobility in poly(3-hexylthiophene). *Appl. Phys. Lett.* **100**, 143303 (2012).
31. I. Salzmann, G. Heimel, M. Oehzelt, S. Winkler, N. Koch, Molecular electrical doping of organic semiconductors: Fundamental mechanisms and emerging dopant design rules. *Acc. Chem. Res.* **49**, 370–378 (2016).
32. J. Gao, E. T. Niles, J. K. Grey, Aggregates promote efficient charge transfer doping of poly(3-hexylthiophene). *J. Phys. Chem. Lett.* **4**, 2953–2957 (2013).
33. S. N. Patel, A. M. Glaudell, D. Kiefer, M. L. Chabinyc, Increasing the thermoelectric power factor of a semiconducting polymer by doping from the vapor phase. *ACS Macro Lett.* **5**, 268–272 (2016).
34. A. M. Glaudell, J. E. Cochran, S. N. Patel, M. L. Chabinyc, Impact of the doping method on conductivity and thermopower in semiconducting polythiophenes. *Adv. Energy Mater.* **5**, 1401072 (2015).
35. D. T. Scholes, S. A. Hawks, P. Y. Yee, H. Wu, J. R. Lindemuth, S. H. Tolbert, B. J. Schwartz, Overcoming film quality issues for conjugated polymers doped with F_4TCNQ by solution sequential processing: Hall effect, structural, and optical measurements. *J. Phys. Chem. Lett.* **6**, 4786–4793 (2015).
36. I. E. Jacobs, E. W. Aasen, J. L. Oliveira, T. N. Fonseca, J. D. Roehling, J. Li, G. Zhang, M. P. Augustine, M. Mascal, A. J. Moulé, Comparison of solution-mixed and sequentially processed P3HT:F4TCNQ films: Effect of doping-induced aggregation on film morphology. *J. Mater. Chem. C* **4**, 3454–3466 (2016).
37. K. Kang, S. Watanabe, K. Broch, A. Sepe, A. Brown, I. Nasrallah, M. Nikolka, Z. Fei, M. Heeney, D. Matsumoto, K. Marumoto, H. Tanaka, S.-i. Kuroda, H. Sirringhaus, 2D coherent charge transport in highly ordered conducting polymers doped by solid state diffusion. *Nat. Mater.* **15**, 896–902 (2016).
38. J. E. Cochran, M. J. N. Junk, A. M. Glaudell, P. L. Miller, J. S. Cowart, M. F. Toney, C. J. Hawker, B. F. Chmelka, M. L. Chabinyc, Molecular interactions and ordering in electrically doped polymers: Blends of PBTTT and F_4TCNQ. *Macromolecules* **47**, 6836–6846 (2014).
39. J. Li, C. W. Rochester, I. E. Jacobs, S. Friedrich, P. Stroeve, M. Riede, A. J. Moulé, Measurement of small molecular dopant F4TCNQ and $C_{60}F_{36}$ diffusion in organic bilayer architectures. *ACS Appl. Mater. Interfaces* **7**, 28420–28428 (2015).
40. I. McCulloch, M. Heeney, C. Bailey, K. Genevicius, I. MacDonald, M. Shkunov, D. Sparrowe, S. Tierney, R. Wagner, W. Zhang, M. L. Chabinyc, R. J. Kline, M. D. McGehee, M. F. Toney, Liquid-crystalline semiconducting polymers with high charge-carrier mobility. *Nat. Mater.* **5**, 328–333 (2006).
41. M. L. Chabinyc, M. F. Toney, R. J. Kline, I. McCulloch, M. Heeney, X-ray scattering study of thin films of poly(2,5-bis(3-alkylthiophen-2-yl)thieno[3,2-*b*]thiophene). *J. Am. Chem. Soc.* **129**, 3226–3237 (2007).

42. B. A. Collins, J. E. Cochran, H. Yan, E. Gann, C. Hub, R. Fink, C. Wang, T. Schuettfort, C. R. McNeill, M. L. Chabinyc, H. Ade, Polarized X-ray scattering reveals non-crystalline orientational ordering in organic films. *Nat. Mater.* **11**, 536–543 (2012).
43. P. Brocorens, A. Van Vooren, M. L. Chabinyc, M. F. Toney, M. Shkunov, M. Heeney, I. McCulloch, J. Cornil, R. Lazzaroni, Solid-state supramolecular organization of polythiophene chains containing thienothiophene units. *Adv. Mater.* **21**, 1193–1198 (2009).
44. T. Schuettfort, B. Watts, L. Thomsen, M. Lee, H. Sirringhaus, C. R. McNeill, Microstructure of polycrystalline PBTTT films: Domain mapping and structure formation. *ACS Nano* **6**, 1849–1864 (2012).
45. D. M. DeLongchamp, R. J. Kline, Y. Jung, D. S. Germack, E. K. Lin, A. J. Moad, L. J. Richter, M. F. Toney, M. Heeney, I. McCulloch, Controlling the orientation of terraced nanoscale "ribbons" of a poly(thiophene) semiconductor. *ACS Nano* **3**, 780–787 (2009).
46. K. Kanai, K. Akaike, K. Koyasu, K. Sakai, T. Nishi, Y. Kamizuru, T. Nishi, Y. Ouchi, K. Seki, Determination of electron affinity of electron accepting molecules. *Appl. Phys. A* **95**, 309–313 (2009).
47. A. Mityashin, Y. Olivier, T. Van Regemorter, C. Rolin, S. Verlaak, N. G. Martinelli, D. Beljonne, J. Cornil, J. Genoe, P. Heremans, Unraveling the mechanism of molecular doping in organic semiconductors. *Adv. Mater.* **24**, 1535–1539 (2012).
48. N. C. Miller, E. Cho, M. J. N. Junk, R. Gysel, C. Risko, D. Kim, S. Sweetnam, C. E. Miller, L. J. Richter, R. J. Kline, M. Heeney, I. McCulloch, A. Amassian, D. Acevedo-Feliz, C. Knox, M. R. Hansen, D. Dudenko, B. F. Chmelka, M. F. Toney, J.-L. Brédas, M. D. McGehee, Use of X-ray diffraction, molecular simulations, and spectroscopy to determine the molecular packing in a polymer-fullerene bimolecular crystal. *Adv. Mater.* **24**, 6071–6079 (2012).
49. C. Wang, D. H. Lee, A. Hexemer, M. I. Kim, W. Zhao, H. Hasegawa, H. Ade, T. P. Russell, Defining the nanostructured morphology of triblock copolymers using resonant soft X-ray scattering. *Nano Lett.* **11**, 3906–3911 (2011).
50. J. Stöhr, *NEXAFS Spectroscopy*, vol. 25 of *Springer Series in Surface Sciences* (Springer, 1992).
51. D. S. Pearson, P. A. Pincus, G. W. Heffner, S. J. Dahman, Effect of molecular weight and orientation on the conductivity of conjugated polymers. *Macromolecules* **26**, 1570–1575 (1993).
52. X. Xue, G. Chandler, X. Zhang, R. J. Kline, Z. Fei, M. Heeney, P. J. Diemer, O. D. Jurchescu, B. T. O'Connor, Oriented liquid crystalline polymer semiconductor films with large ordered domains. *ACS Appl. Mater. Interfaces* **7**, 26726–26734 (2015).
53. J. Li, C. W. Rochester, I. E. Jacobs, E. W. Aasen, S. Friedrich, P. Stroeve, A. J. Moulé, The effect of thermal annealing on dopant site choice in conjugated polymers. *Org. Electron.* **33**, 23–31 (2016).
54. J. Fuzell, I. E. Jacobs, S. Ackling, T. F. Harrelson, D. M. Huang, D. Larsen, A. J. Moulé, Optical dedoping mechanism for P3HT:F4TCNQ mixtures. *J. Phys. Chem. Lett.* **7**, 4297–4303 (2016).
55. I. E. Jacobs, F. Wang, N. Hafezi, C. Medina-Plaza, T. F. Harrelson, J. Li, M. P. Augustine, M. Mascal, A. J. Moulé, Quantitative dedoping of conductive polymers. *Chem. Mater.* **29**, 832–841 (2017).
56. S. D. Kang, G. J. Snyder, Charge-transport model for conducting polymers. *Nat. Mater.* **16**, 252–257 (2017).
57. D. Wang, W. Shi, J. Chen, J. Xi, Z. Shuai, Modeling thermoelectric transport in organic materials. *Phys. Chem. Chem. Phys.* **14**, 16505–16520 (2012).
58. G. Zuo, H. Abdalla, M. Kemerink, Impact of doping on the density of states and the mobility in organic semiconductors. *Phys. Rev. B* **93**, 235203 (2016).
59. Q. Wei, M. Mukaida, K. Kirihara, T. Ishida, Experimental studies on the anisotropic thermoelectric properties of conducting polymer films. *ACS Macro Lett.* **3**, 948–952 (2014).
60. S. Qu, Q. Yao, L. Wang, Z. Chen, K. Xu, H. Zeng, W. Shi, T. Zhang, C. Uher, L. Chen, Highly anisotropic P3HT films with enhanced thermoelectric performance via organic small molecule epitaxy. *NPG Asia Mater.* **8**, e292 (2016).
61. O. Bubnova, Z. U. Khan, H. Wang, S. Braun, D. R. Evans, M. Fabretto, P. Hojati-Talemi, D. Dagnelund, J.-B. Arlin, Y. H. Geerts, S. Desbief, D. W. Breiby, J. W. Andreasen, R. Lazzaroni, W. M. Chen, I. Zozoulenko, M. Fahlman, P. J. Murphy, M. Berggren, X. Crispin, Semi-metallic polymers. *Nat. Mater.* **13**, 190–194 (2013).
62. M. N. Gueye, A. Carella, N. Massonnet, E. Yvenou, S. Brenet, J. Faure-Vincent, S. Pouget, F. Rieutord, H. Okuno, A. Benayad, R. Demadrille, J.-P. Simonato, Structure and dopant engineering in PEDOT thin films: Practical tools for a dramatic conductivity enhancement. *Chem. Mater.* **28**, 3462–3468 (2016).
63. C. K. Chiang, C. R. Fincher Jr., Y. W. Park, A. J. Heeger, H. Shirakawa, E. J. Louis, S. C. Gau, A. G. MacDiarmid, Electrical conductivity in doped polyacetylene. *Phys. Rev. Lett.* **39**, 1098–1101 (1977).
64. X. Wang, V. Ho, R. A. Segalman, D. G. Cahill, Thermal conductivity of high-modulus polymer fibers. *Macromolecules* **46**, 4937–4943 (2013).
65. A. Weathers, Z. U. Khan, R. Brooke, D. Evans, M. T. Pettes, J. W. Andreasen, X. Crispin, L. Shi, Significant electronic thermal transport in the conducting polymer poly(3,4-ethylenedioxythiophene). *Adv. Mater.* **27**, 2101–2106 (2015).
66. H. Ushirokita, H. Tada, In-plane thermal conductivity measurement of conjugated polymer films by membrane-based AC calorimetry. *Chem. Lett.* **45**, 735–737 (2016).
67. J. Liu, X. Wang, D. Li, N. E. Coates, R. A. Segalman, D. G. Cahill, Thermal conductivity and elastic constants of PEDOT:PSS with high electrical conductivity. *Macromolecules* **48**, 585–591 (2015).
68. I. Mcculloch, M. Heeney, M. L. Chabinyc, D. Delongchamp, R. J. Kline, M. Cölle, W. Duffy, D. Fischer, D. Gundlach, B. Hamadani, R. Hamilton, L. Richter, A. Salleo, M. Shkunov, D. Sparrowe, S. Tierney, W. Zhang, Semiconducting thienothiophene copolymers: Design, synthesis, morphology, and performance in thin-film organic transistors. *Adv. Mater.* **21**, 1091–1109 (2009).
69. J. Ilavsky, Nika: Software for two-dimensional data reduction. *J. Appl. Cryst.* **45**, 324–328 (2012).

Acknowledgments: Use of the SSRL, SLAC National Accelerator Laboratory, is supported by the U.S. Department of Energy, Office of Science, Office of Basic Energy Sciences, under contract no. DE-AC02-76SF00515. This research used resources of the ALS, which is a U.S. Department of Energy Office of Science User Facility under contract no. DE-AC02-05CH11231. The MRL Shared Experimental Facilities are supported by the MRSEC Program of the NSF under award no. DMR 1121053, a member of the NSF-funded Materials Research Facilities Network. **Funding:** The authors acknowledge the support of the Air Force Office of Scientific Research through the Multidisciplinary University Research Initiative on Controlling Thermal and Electrical Transport in Organic and Hybrid Materials (AFOSR FA9550-12-1-0002). A.M.G. received partial support from the ConvEne IGERT Program of the NSF under NSF-DGE 0801627. E.L. acknowledges support from the NSF Graduate Research Fellowship (DGE-1144085).
Author contributions: S.N.P. designed and performed all experiments related to thermoelectric measurements, GIWAXS, and RSoXS and wrote the manuscript with input from M.L.C. A.M.G. assisted in thermoelectric measurements and assisted in the analysis of the data. K.A.P. performed UV-vis-NIR experiments. E.M.T. performed AFM experiments. K.A.O. performed high-resolution x-ray scattering experiments. E.L. assisted with RSoXS experiments. M.L.C. supervised all aspects of the project, designed experiments, and was involved in writing of the manuscript. All coauthors assisted with writing and editing of the manuscript. Figure credit: S.N.P. for Figs. 1, 3, and 4; S.N.P., K.A.P., E.M.T., and A.M.G. for Fig. 2; S.N.P. and E.L. for Figs. 5 and 6; S.N.P. and A.M.G. for Fig. 7. **Competing interests:** The authors declare that they have no competing interests. **Data and materials availability:** All data needed to evaluate the conclusions in the paper are present in the paper and/or the Supplementary Materials. Additional data related to this paper may be requested from the authors.

Submitted 9 February 2017
Accepted 28 April 2017
Published 16 June 2017
10.1126/sciadv.1700434

Citation: S. N. Patel, A. M. Glaudell, K. A. Peterson, E. M. Thomas, K. A. O'Hara, E. Lim, M. L. Chabinyc, Morphology controls the thermoelectric power factor of a doped semiconducting polymer. *Sci. Adv.* **3**, e1700434 (2017).